SOFT ROBOTICS
Volume 00, Number 00, 2025

DOI: 10.1089/soro.2024.0141

SoRo
Soft Robotics

Open camera or QR reader and scan code to access this article and other resources online.

ORIGINAL ARTICLE

A Holistic Indirect Contact Identification Method for Soft Robot Proprioception

Shuoqi Wang,[1] Keng-yu Lin,[2] Xiangru Xu,[1] and Michael Wehner[3]

Abstract

Soft robots hold great promise but are notoriously difficult to control due to their compliance and backdrivability. In order to implement useful controllers, improved methods of perceiving robot pose (position and orientation of the entire robot body) in free and perturbed states are needed. In this work, we present a holistic approach to robot pose perception in free bending and with external contact, using multiple soft strain sensors on the robot (not collocated with the point of contact). By comparing the deviation of these sensors from their value in an unperturbed pose, we are able to perceive the mode and magnitude of deformation and thereby estimate the resulting perturbed pose of the soft actuator. We develop a sample 2 degree-of-freedom soft finger with two sensors, and we characterize sensor response to front, lateral, and twist deformation to perceive the mode and magnitude of external perturbation. We develop a data-driven model of free-bending deformation, we impose our perturbation perception method, and we demonstrate the ability to perceive perturbed pose on a single-finger and a two-finger gripper. Our holistic contact identification method provides a generalizable approach to perturbed pose perception needed for the control of soft robots.

Keywords: multidirectional PneuNet actuator, actuator with embedded sensing, pose estimation, indirect contact sensing

Introduction

The emerging field of soft robots challenges the traditional perception of robots as rigid, inflexible machines. Unlike conventional robots made with hard materials, soft robots are typically constructed from materials with relatively low elastic modulus, such as elastomers,[1] hydrogels,[2] flexible polymers,[3] and fabrics.[4] The choice of materials grants them better flexibility and adaptability, extending the capabilities of robots into entirely new domains.[5,6] In contrast to rigid-link robots, actuating at discrete joints, soft robots possess inherent deformability allowing them to traverse different terrains during exploration tasks,[7] and adapt to diverse body morphologies in rehabilitation applications.[8,9] Moreover, the compliance of soft robots allows them to deflect in response to external force and moment (Fig. 1) for safer interactions with their surroundings compared with rigid robots. Their materials naturally absorb shock from contact, minimizing potential damage to themselves and their surroundings. Consequently, soft robots are well suited for interacting with humans, handling fragile objects, and operating in sensitive and unstructured environments.[10]

Despite holding great promise, soft robots have yet to see wide commercial acceptance, due in large part to challenges

[1]Department of Mechanical Engineering, University of Wisconsin, Madison, Madison, Wisconsin, USA.
[2]Applied Materials, Santa Clara, California, USA.
[3]Wehner Engineering, Madison, Wisconsin, USA.

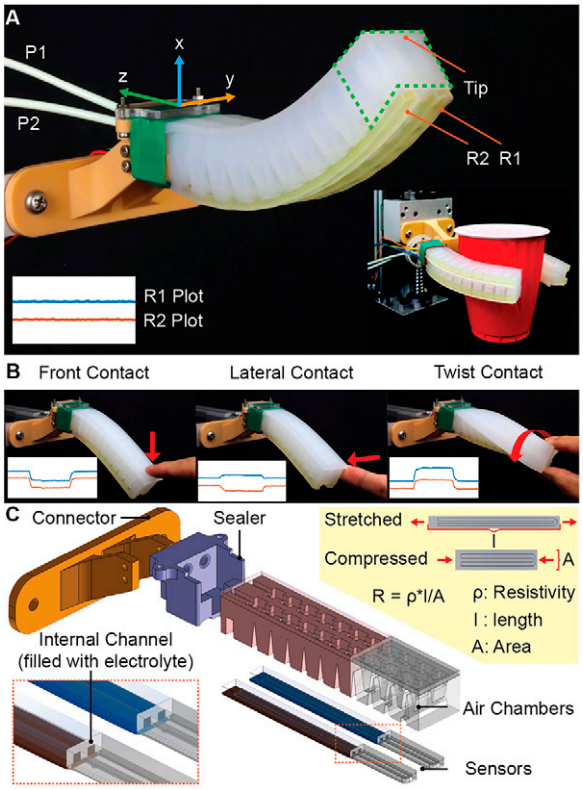

FIG. 1. Sensor-embedded multidirectional pneumatic network actuator (SEMPA). **(A)** Two pressure inputs (*P*1, *P*2) inflate parallel chambers along the length of the finger. Two resistive sensors (*R*1, *R*2) perceive deformation (resistance plots, lower left). A two-finger gripper is shown holding a cup (*lower right*). Each SEMPA finger is 115 mm in length. **(B)** Illustration of three modes of contact and the corresponding sensors' responses. By comparing the two sensor responses, we can identify the perturbation mode. **(C)** Exploded view of the SEMPA and its internal structure, with the mechanics of the embedded soft sensors (*upper right*).

in control.[11] Effective robot control requires perception of the robot's position and configuration, similar to our brains' use of sensory input for proprioception to make decisions.[12] For effective control, robots must be able to perceive their pose (overall position and orientation of all robot parts relative to one another and in space). For a conventional robot consisting of rigid links actuating at discrete degrees of freedom (DOF), pose estimation is well understood and is generally calculated with information from one sensor at each rotational or translational joint. However, soft robots, with their continuum mechanics and theoretically infinite DOF,[13] do not lend themselves to rigid body models. Additionally, traditional robots can often neglect complex dynamics and mechanics, such as resonance and link deformation, because deviation from the rigid body model is negligible. In contrast, by their very design, soft robots are both flexible and back-drivable. While an actuator's geometry may be predictable in free bending (continuum actuation with no external forces), its shape changes greatly in response to external loads (unanticipated contact, payload mass, or even deflection due to gravity). Therefore, accurate proprioception of a soft robot requires drastically more system information to determine pose, especially under load from various external forces and moments. To address this, the field of soft robotics requires modeling and sensing a broad range of external contacts.

Modeling

There have been numerous methods used to estimate the pose of soft robots.[14] Analytical modeling involves studying the kinematic and dynamic equations of soft robots, typically based on simplifying assumptions.[15] Common analytical models include pseudo rigid body approximation,[16,17] Cosserat rods approximation,[18] or piecewise constant curvature approximation.[19] While useful in some cases, these models do not guarantee close correlation with real applications, as they generally consider only free-bending scenarios.[20,21] While some models account for external loading and contact, they require precise knowledge of contact location and direction, limiting their effectiveness in unstructured environments.[22,23]

An alternative solution that better captures the nonlinear elasticity of material and contact interaction is finite element analysis (FEA).[24–26] FEA divides the geometry of soft robots into meshes to make estimations, but its accuracy is highly sensitive to material and structural parameters. While some real-time FEA control has been achieved using model order reduction,[27–29] there remains a trade-off between computational complexity and accuracy.[30] A more detailed model requires far more computational resources.

Data-driven methods, utilizing external or embedded sensors, fit models or train neural networks using sensory data.[31,32] These methods encompass statistical techniques such as linear regression,[33] support vector regression,[34] and Gaussian process regression.[35] For more complex data, machine learning methods like multilayer perception[34] and recurrent neural network can be employed.[36] While these approaches can model complex behaviors, they are highly sensitive to data and may struggle with long-term dynamic changes. Additionally, data-driven models often provide less intuitive insights into the underlying physics of soft robots.

These modeling techniques have provided promising results in ideal conditions (free bending and scenarios with very specific/well-defined contacts). However, robust methods of controlling soft robots in general conditions remain elusive. Such control, covering a broad spectrum of soft robots in the real world, will not be possible without a robust perception of robot pose.[15,37,38] This requires accurate real-time proprioception of deformation from the myriad likely external forces. We present a novel, holistic sensing approach to proprioception, fundamentally designed around the deformability of soft robots. This method fills a critical gap in the field, allowing soft robots to perceive and respond to a broad range of external forces by comparing responses of internal sensors not collocated with the points of contact.

Sensing

In most traditional rigid robot kinematic models, a sensor is typically dedicated to measuring a specific variable. For example, a rotational encoder is placed at a rotation degree of freedom to sense joint angle, and a pressure sensor is placed at the anticipated location of contact to sense contact pressure. If one more phenomenon is to be perceived, one

more sensor is added to the robot. A similar strategy has been employed in soft robots.[39,40] Embedded sensors, integrated directly into soft actuators, measure electrical signals like resistance,[39,41] capacitance,[42,43] or optical signal,[44,45] to estimate strain, stress, or contact. These sensors are usually calibrated to extract information on a single phenomenon. As the number of phenomena of interest grows, this presents a great challenge in real-time signal processing and fabrication, as the number of required sensors is equal to or greater than the number of phenomena of interest. It is also not clear what configuration or density of sensors would be needed to sense a contact that is continuously varying in size and location (common in continuously deformable soft robots). E-skins offer a potential solution by stacking multiple sensors sensitive to different stimuli.[46–49] These skins require direct contact and an extensive sensor array to cover large areas, making them impractical for mass production and real-time computation. Additionally, reliance on a single signal can lead to nonunique mappings, where many behaviors result in the same response. All of these sensors focus on isolating individual phenomena, often requiring sensors to be shielded from the "noise" caused by deformations/motions from other parts of the soft robot.[40] External sensors, such as vision systems, have also been used in soft robots but are prone to ambient occlusion and high computational costs.[37]

Indirect sensing/proprioceptive sensing

Proprioceptive perception in soft robotics extends beyond sensor development, focusing on interpreting sensor data into meaningful pose information such as position and contact detection. Several studies have integrated sensors to estimate the state of actuators.[50,51] In our previous work,[52–55] we presented a planar actuator capable of detecting frontal contact by tracking resistance in a dorsally mounted bend sensor versus a single input pressure. Upon contact with an external object, the actuator would deflect from its free-bending state, causing the resistance of the bending-sensitive sensor to deviate from its expected value. When this deviation exceeded the threshold, contact was declared. Other notable examples of indirect sensing include strain sensors in parallel with soft actuators using a bioinspired approach to sense contact,[56] wave guides to sense bending and contact of an actuator,[57] a microfiber-based sensor integrated within an actuator enabling feedback control,[58] and an acoustic sensor used to recognize the change in sound corresponding to the change in bending curvature of the actuator, thereby identifying contact and mapping it to a specific location.[59,60]

Additionally, machine learning has enhanced proprioceptive perception in sensor-embedded soft actuator. Loo et al.[61] used machine learning to map pressure and embedded curvature sensor data to bending angles and contact forces in a robot. She et al.[62] trained a neural net with embedded camera images to estimate the two-dimensional (2D) position and classify the object in contact. Similar strategies have been demonstrated using other embedded sensors,[63,64] leveraging indirect sensing approaches to avoid the need for numerous sensors or direct sensor contact. While these works are promising, they primarily focus on detecting the presence or absence of contact without identifying deformation type or magnitude. In real unstructured environments, however, external contact can occur unpredictably in terms of locations, directions, or form, significantly affecting soft robot pose. To fully harness the proprioception of soft robot for real-world tasks, a comprehensive understanding of external contacts and their impact on robot deformation is essential. We present an approach in which we compare the responses of several sensors to holistically determine the pose of the robot system under contact.

Holistic sensing, our approach

In our previous work,[65] we found that the state of one part of the Octobot system affected performance throughout the device. In our initial exploration of sensorized elastomeric fingers,[40] we found that deformation (deliberate actuation or external perturbation) in one part of the system caused sensor responses throughout the robot, interfering with the ability to independently sense phenomena of interest. By their very nature, soft robots deform, causing interaction between subsystems. The fundamental inspiration behind the work presented here is to use this noise or "cross-talk" between sensors and actuators, not as noise to be overcome, but as a valuable source of system information. We believe that, when properly designed, more information can be obtained from sensor responses holistically than from the sum of the individual sensors.

To achieve this, we introduce a holistic indirect contact identification (HICI) method. By comparing the responses of several sensors, HICI allows us to perceive contact and identify phenomena that could not be perceived by any individual sensor. Due to their inherent deformability, the subsystems in soft robots are notoriously interconnected, with actions in one part of the system causing sensor responses and changes in actuator behavior throughout the robot.[40,65] We take inspiration from embodied intelligence (using external interaction information to simplify control),[66,67] and from proprioception in nature to use these distributed signals, not as a source of noise to be minimized, but as a source of valuable state information. Further, by embracing this indirect contact method, we perceive all these contact events without requiring colocation between the sensor and the area of contact. This is key in soft robotics, as contact can be spread across an unknown and often varying region of the robot, making direct contact perception infeasible. This holistic contact method allows us to differentiate between a variety of unknown external loads and to estimate the resulting deformation and pose in a static or quasistatic state. This method does not consider high-speed operation, in which system dynamics, transient sensor response, or lag in perception may become an appreciable part of the signal. However, high-speed operation is generally not the primary operating domain of soft robot grippers. Because our scheme does not change the existing model of a soft robot, it can be combined with any model that characterizes robot pose in free bending, thereby achieving real-time proprioception in both free bending and contact conditions. We believe HICI has the potential to bring true proprioception to soft robots, enabling them to perform practical tasks and evolve into real-world devices with capabilities on par with traditional robots.

Sensor-embedded multidirectional pneumatic network actuator

To demonstrate our method, we introduce a sensor-embedded multidirectional pneumatic network actuator (SEMPA), as shown in Figure 1A–C. The SEMPA includes two parallel lines of inflatable chambers along its length and two embedded fluidic sensors on its dorsal side. By comparing the responses from the two embedded sensors, $R1$ and $R2$, we can use HICI to distinguish multiple contact modes: front contact, lateral contact, and twist contact (Fig. 1B) encountered by the SEMPA.

Key contributions of this work

Soft robots deform under external loading, often in complex modes, making it difficult for the community to model, predict, and even measure their pose. Similarly, sensors in soft robots (each intended to perceive one phenomenon of interest), tend to respond to unrelated deformations from entirely different parts of the system. Our method embraces this complex motion and inherent cross-talk, eschewing the traditional one-sensor-per-phenomenon method in favor of a holistic pose perception approach. This novel method will greatly affect the soft robotics field, bringing key contributions of:

- *Contact detection in 3D, without a contact sensor, via deviation from anticipated sensor values.* We present a method (HICI) to determine external contact by comparing the states of multiple soft sensors mounted throughout the soft actuator. Several studies described above use individual sensors to sense individual soft robotic phenomena. In our comparison-based method, we utilize the compliance characteristic in soft robots to holistically sense deformation by deviations of signals throughout the system from their anticipated values. We demonstrate the ability to perceive intentional contact (gripping an object) and unintentional contact (perturbation in several directions as well as changing load of a carried object). This deviation-based method has the additional advantage of not requiring a dedicated "contact" sensor or a sensor collocated with the anticipated point of contact.
- *Pose estimation by comparing multiple sensors.* Building on our HICI approach, we enhance the capability of a data-driven model, extending its application from characterizing free bending to capturing actuator behavior under external contact. By tracking deviations of both sensors from their anticipated values, the model can detect external contact and determine the resulting pose of the actuator under such conditions. We determine the direction from which a contact occurred and the magnitude of resulting displacement in 3D space. We demonstrate a finger's ability to sense the magnitude of bend, twist, and lateral deformation, updating its pose in response to these interactions.
- *An approach applicable to most forms of soft robots.* While we primarily demonstrate our approach on the one-finger motif, the approach can be applied to most underactuated systems in which multiple deflection sensors can be applied. This approach is particularly useful for elastomeric pneumatic soft robots, which we demonstrate with data on actuators with several other sensor schemes, preliminary results on other actuators (explored in our previous works), and a two-finger gripper motif, serving as a baseline for extending the approach to a wide range of soft grippers.

In this article, we first use the HICI method to characterize the response of an SEMPA to various modes of perturbation. We then develop a data-driven model for SEMPA in free bending and incorporate it with HICI results to estimate the SEMPA's pose under unknown external loading. Finally, we present a case study in which a 2-finger gripper perceives and responds to external forces, showcasing the generalizability of the HICI method.

The article is organized as follows: Following this Introduction section, we present Results section, including design and characterization of the device, the HICI method, and integration with a data-driven model. Next, we present Materials and Methods section describing the details of our manufacturing process and experiment methodology. We conclude with a Discussion and Conclusion section of the significance of our method, its impact on the field, and the next steps.

Results

Design and detecting perturbation mode in free bending

The widely used Pneumatic Network (PneuNet) actuator design consists of an elastomeric finger-like body containing an internal air bladder consisting of a series of hollow chambers along its length. Typically, one surface of the actuator is reinforced with fabric or an elastomer of higher modulus. When pressurized, the air chambers bulge and exert force against each other, causing the actuator to bend toward the less stretchable side.[68–70] Traditional PneuNets bend in a single (planar) direction, but other forms have been developed such as bidirectional,[71,72] multidirectional,[73,74] and omnidirectional[75–77] actuators. Our SEMPA is a multidirectional PneuNet actuator, incorporating two parallel air chambers along its length (Fig. 2A), inflated with two separate air supplies, $P1$ and $P2$ (Fig. 1A). Based on the input pressure $P1$ and $P2$, the SEMPA can bend both in-plane and out-of-plane. Primarily intended for gripping, out-of-plane deformation of the SEMPA was designed to (1) provide sufficient out-of-plane motion to adapt grip if planar actuation yields suboptimum contact and (2) provide out-of-plane force to counteract perturbations (see Supplementary videos SV1, video SV2). The goal was not to maximize out-of-plane deformation. By inflating both chambers ($P1 = P2$), the finger will actuate in the xz plane (Fig. 2B). Biasing inflation in favor of one chamber ($P1 \neq P2$) will increase actuation on that side, and the finger will actuate out of the xz plane. At the extreme (either $P1$ or $P2 = 0$), the finger will deflect approximately $\pm 20°$ out of plane (Fig. 2B), sufficient to adapt grip or to counteract external perturbations (see Supplementary Video S2).

Two soft fluidic resistive sensors are adhered to the dorsal surface of the SEMPA symmetrically near its left and right edges. The sensors filled with the electrolyte solution 1-ethyl-3-methylimidazolium ethyl sulfate (Sigma Aldrich, Burlington, MA, USA)[40] are highly stretchable. As the

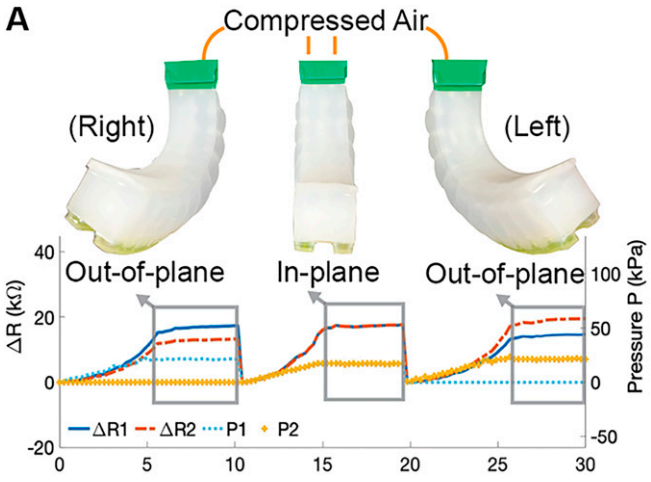

FIG. 2. Free bending and sensor response of an SEMPA actuator. **(A)** Bending behaviors (in-plane and out-of-plane bending) of SEMPA under different inflation conditions, *Top*: photos of actuator bending. *Bottom*: plot of sensor responses ($\Delta R1$, $\Delta R2$) to varying input pressure states ($P1$, $P2$). **(B)** Illustration of motion space of conventional unidirectional PneuNet actuators (constrained to xz plane) and SEMPA (out-of-plane actuation to ±20°).

length and cross-section area of the sensors' internal channel change with the movement of the actuator, such as bending or twisting, the sensors' resistance will vary accordingly, following the resistance equation $R = \rho * (L/A)$, where ρ is the resistivity, L is the length, and A is the cross-sectional area of the internal channel of the sensor. We have used this approach to sensing deformation in the past to perceive bending, contact, and inflation pressure,[40] and our preliminary work.[55] Sensor resistance varies with time, which is believed to be due to the migration of ambient moisture through the elastomer and into the sensor channels. All of our experiments were conducted on sensors more than 14 days old, at which point resistance has been shown to reach a steady state. Details on the time-resistance relationship are in our previous work.[40] An overview of the finger's mechanical design is shown in Figure 1C, and fabrication is described in the Materials and Methods section. An explanation of the underlying asymmetrical actuation concept and the electronic circuit (including specifics of the relaxation oscillator) is covered in detail in our previous work.[55] When the SEMPA actuates in-plane, the dorsal surface becomes longer, stretching both sensors equally, yielding similar increases in sensor resistance. When the SEMPA actuates out-of-plane (one side actuates more than the other), the sensors deform by unequal amounts, resulting in unequal changes in resistance. Maximizing the distance between the sensors (while still on the dorsal surface) maximizes the difference in sensor response to out-of-plane actuation, increasing sensitivity. When input pressure follows $P1 > P2$, change in output resistance $\Delta R1 > \Delta R2$; when $P1 < P2$, $\Delta R1 < \Delta R2$; and when $P1 = P2$, $\Delta R1 \approx \Delta R2$ (Fig. 2A). Tracking these sensor resistances allows us to track SEMPA actuation during unperturbed free-bending. In a future section of this work, we generate a free-bending model, mapping sensor responses ($R1$, $R2$) for the range of unperturbed poses (actuator orientations and pressure states). Critical for this work, the sensors also experience resistance change when the SEMPA is deflected due to an external force. By comparing the deviation of both sensors from their value in an unperturbed pose, we are able to perceive the mode and magnitude of deformation and thereby estimate the resulting perturbed pose of the SEMPA.

Experimental setup

We controlled the SEMPA with the system shown in Figure 3. All pneumatic solenoid valves were connected to a single pressure regulator, controlled by an Arduino microcontroller through four corresponding Negative Positive Negative (NPN) transistors, powered by an external power supply. The resistances of the soft sensors were measured utilizing a relaxation oscillator, which produced signals with varying frequencies depending on the sensor's resistance. By utilizing the known input frequency (f), circuit capacitance (C), and the overall resistance (R_o) used in the relaxation oscillator, the sensor resistance (R) was calculated using the following equation.[55]

$$R = \frac{1}{2 \times f \times C \times ln\left(\frac{1+R_o}{1-R_o}\right)} \quad (1)$$

With this experimental setup, we controlled input pressures ($P1$, $P2$) and recorded changes in output resistances ($\Delta R1$, $\Delta R2$). Note that all sensor values were collected during the flexion portion of the actuation cycle (slow increasing pressure). The flexion phase of the soft actuator is prioritized, as it performs the primary functional tasks of a soft gripper (establishing and then maintaining a grasp of

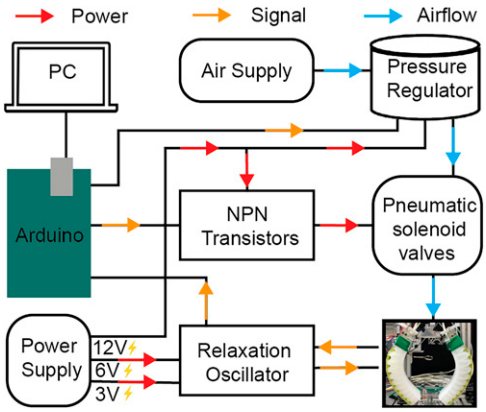

FIG. 3. Schematic of the overall two-finger system with four solenoid valves and relaxation oscillators. A single SEMPA finger uses a similar configuration, with only two solenoid valves and relaxation oscillators.

external objects), while the relaxation phase mainly resets the system for subsequent cycles.

Detecting mode of contact

In our previous work, we demonstrated the ability of a planar PneuNet actuator with a single dorsal curvature sensor to detect front contact. When the sensor's signal deviated from a reference value beyond a predetermined threshold, the actuator had contacted an external object (assumed to be near the front and tip of the finger, as this was perceived during a tapping motion). This proof of concept served as a foundation toward the work presented here. In this work, we characterize deformation from various modes of contact using our HICI method, and we estimate soft robot pose in free bending and under perturbation. In this method, we focus not on the signal from one sensor but on comparing the signals between multiple sensors. As more sensors are designed into a soft robot system (particularly a multi-DOF robot), more detailed pose and contact information can be obtained, resulting in a better understanding of the type of contact, the direction of force, and the resulting perturbed pose of the robot.

By characterizing the patterns of the two SEMPA sensors, we can distinguish three distinct types of contacts: front contact, lateral contact, and twist contact.

1. Front contact: An external force along the negative x-axis is applied on the front surface of the SEMPA (one pressure state in Fig. 4A, B; other states in Supplementary Figs. S1, Figs. S2).
2. Lateral contact: An external force along the positive/negative y-axis is applied at the side of the tip of the

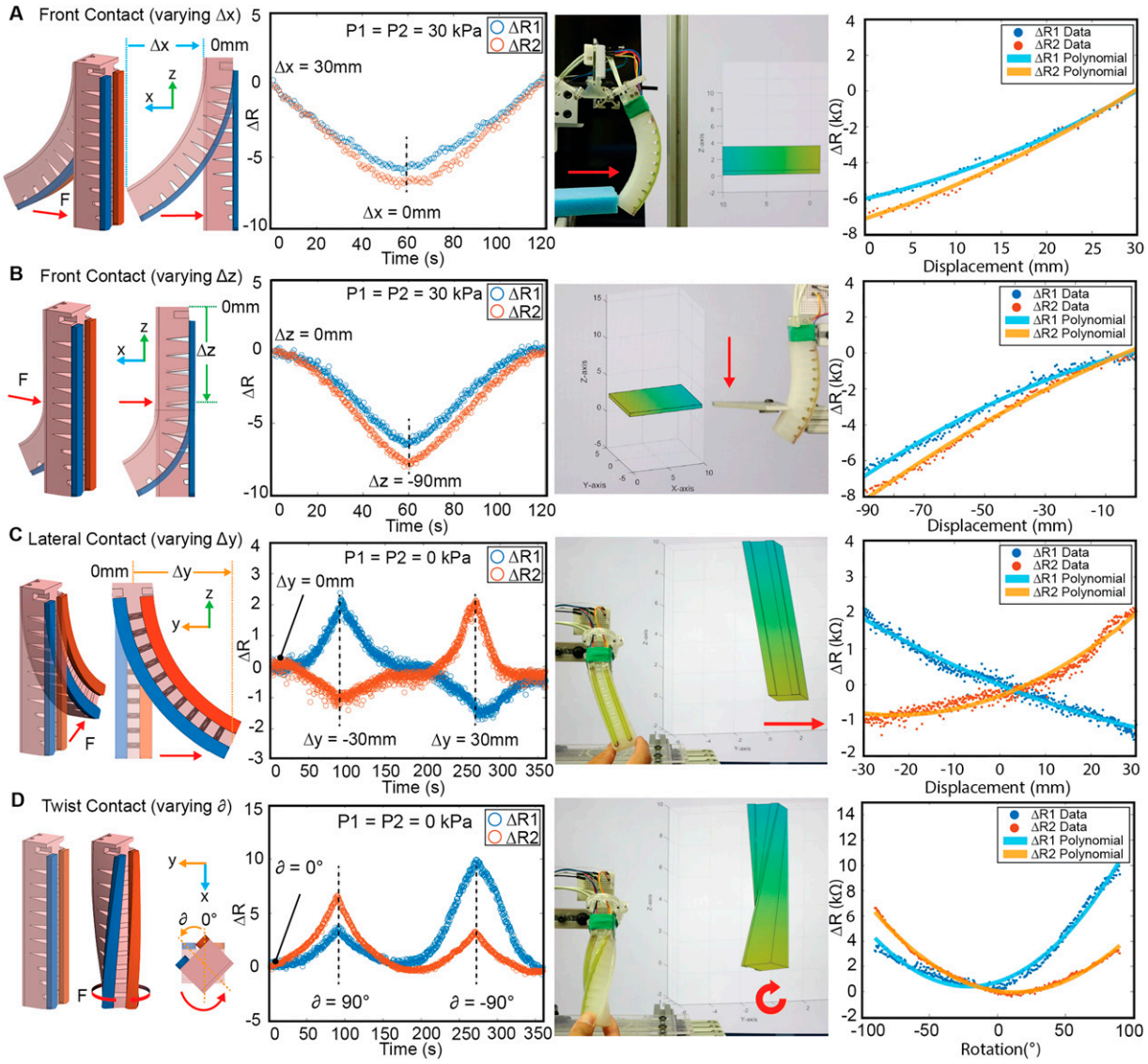

FIG. 4. Characterizing SEMPA response to various perturbation modes (selected pressure states shown here. All other pressure states detailed in Supplementary Figs. S1, S2, S3, and S4). From *left to right*: Computer Aided Design (CAD) plot of contact. Sensors' responses during contact (ΔR vs. time). Screenshot from the demonstration video (see Supplementary Videos SV3, SV4, and SV5). Sensors' responses (ΔR vs. displacement). **(A)** Front contact (obstacle at tip), $z = -90$ mm, vary obstacle position along the x-axis. **(B)** Front contact, $x = 0$ mm, vary obstacle position along z-axis. **(C)** Lateral contact (*obstacle at the tip*), translate along y-axis. **(D)** Twist contact, rotate tip about z-axis.

SEMPA (one pressure state in Fig. 4C; other states in Supplementary Fig. S3).

3. Twist contact: An external torsion along the positive/negative rotation axis (z-axis if SEMPA is uninflated) is applied at the tip of the SEMPA (one pressure state in Fig. 4D; other states in Supplementary Fig. S4).

Front contact is the common result of planned interactions such as gripping an object. In contrast, lateral and twist contacts are likely to occur due to gripping uneven or irregularly shaped surfaces (asymmetrically gripping an object at an angle). Lateral or twist contact may also occur due to unplanned interaction, such as bumping or an object slipping (or about to slip) from the grip. Thus, it is very desirable to accurately determine the location of the front contact and the size of the object (Fig. 4A, B). It is useful to understand the magnitude of lateral and twist contact (Fig. 4C, D), though the precise location of these contacts may be less crucial.

Front contact. When front contact occurs, both sensors' resistances decrease compared to the initial value ($\Delta R1$, $\Delta R2 < 0$) due to the reduced actuator curvature (Fig. 4A, B). Knowing the pressure inputs ($P1$, $P2$ to SEMPA) and the anticipated outputs ($\Delta R1$, $\Delta R2$), we can estimate the magnitude of the deformation due to front contact. If contact occurs with a known x position, we can estimate the contact location along the z-axis of the finger. Conversely, if contact occurs at a known z position, such as the fingertip, we can estimate the influence of contact on the tip position along the x-axis of the finger.

Constant z, varying x: With the SEMPA inflated to $P1 = P2 = 30$ kPa, we imposed a front perturbation (x = 30 to 0 to 30 mm) at a distance $z = 110$ mm from the base (near the tip) as shown in Figure 4A. We curve-fit the resulting resistance–displacement data to find a second-order linear equation estimating tip frontal displacement with changing x from the changes in $R1$ and $R2$ (Fig. 4A, right).

Constant x, varying z: Next, with the SEMPA inflated to $P1 = P2 = 30$ kPa, we introduced an obstacle at $x = 0$, z = 25 mm (near the base of the sensors, where the SEMPA could no longer perceive small perturbation). We moved the obstacle in the z-direction –90 mm (to the tip of the SEMPA), then back to its original position. We curve-fit the resulting resistance–displacement data to find a second-order linear equation estimating tip frontal displacement with changing z from the changes in $R1$ and $R2$ (Fig. 4B, right).

Lateral contact. When a lateral contact occurs, one sensor's resistance decreases while the other's increases (Fig. 4C). This behavior can be related to classical mechanics, where strain in a beam (ε) in bending is known to vary linearly with distance from the neutral surface (y) and distance to neutral surface from the center of curvature (ρ) in Eq. 2.

$$\varepsilon = \frac{-y}{\rho} \tag{2}$$

Although SEMPA has complex geometry and nonlinear material properties, we can gain a qualitative understanding of sensors' deformations from the equation governing linear displacement in a rectangular beam in the linear elastic region. We imposed a lateral perturbation (y = 0 to –30 to 0 to 30 to 0 mm). Based on the sign of the resistance changes, we determine the direction of the perturbation. If $R1$ increases and $R2$ decreases, the perturbation is acting in the $-y$ direction (Fig. 4C, second plot) and vice versa. We curve-fit the resulting resistance–displacement data to find a second-order linear equation estimating tip lateral displacement from the changes in $R1$ and $R2$ (Fig. 4C, right).

Twist contact. When a twist contact occurs, both sensors' resistances increase (Fig. 4D). Comparing again to solid mechanics, if the SEMPA were a regular rectangular beam of length (L), undergoing twist of angle (∂), and the sensors were at a similar distance from the actuator's central axis (ρ), the sensors would experience equal shear strain (γ) and could be characterized by Eq. 3.

$$\gamma = \frac{\rho \times \partial}{L} \tag{3}$$

The nonuniform SEMPA can be qualitatively compared to this, but geometric and material nonhomogeneity cause quantitative deviation (Fig. 4D, right). We curve-fit the resulting resistance–displacement data to find a second-order linear equation estimating tip twist angle from the changes in $R1$ and $R2$ (Fig. 4D, right).

To further validate the feasibility and performance of our method, we characterized the HICI method with the SEMPA throughout its range of pressure states ($P1$, $P2$) under various poses. Through this characterization, we demonstrate the HICI method to be effective across almost all actuation states within the working pressure range ($P1$, $P2 \in$ 0–40 kPa). The only exceptions are that at maximum pressure ($P1 = P2 = 40$ kPa), the SEMPA shows reduced ability to detect twist contact and loses the ability to detect lateral contact. Resistance versus time curves (equivalent to column 2 in Fig. 4) for the other pressure states are given in Supplementary Figs. S1, S2, S3, and S4). To assess repeatability and accuracy, we performed five trials for each contact scenario, calculating the mean and variance of the results. The findings showed high repeatability and accuracy, with a maximum variance of 0.06 kΩ (Supplementary Fig. S7A). This low variance indicates that the method reliably reproduces sensor readings under identical conditions, underscoring its robustness and potential for consistent contact identification in various real-world applications.

To demonstrate the adaptability of HICI, we tested the method on the SEMPA actuator (design used throughout this work), but with different sensor configurations (Supplementary Fig. S7B, C). The sensor configurations (varying sensor channel cross-section or modifying sensor effective length) yielded different responses during actuation, which could be used for future design refinement to increase sensitivity to desired stimuli or over portions of the actuation cycle. While response magnitude varied, the same overall response modes were seen in all experiments, suggesting that the HICI method could be used with alternate sensor layouts and imposes minimal requirements on specific sensor layouts. Regarding the actuator configuration, while this study focused on a specific multidimensional design, SEMPA, similar finger-sensor configurations have been developed in

several of our previous works. Our early 3D-printed finger demonstrated the deviation of all sensor signals to external perturbation,[40] which served as inspiration for this work. Several other actuator designs were used to develop the threshold-based contact detection model described in the introduction.[55,78] All of these sensorized fingers demonstrated the ability to perceive contact in the same manner. These numerous designs composed of various geometry, actuator configuration, and materials provide encouraging data points that actuator structure and material composition do not prevent the method's successful application. Since all types of contact that have been tested occur passively in response to external stimuli, actuator design is unlikely to influence the detection process. This independence from specific structural or material configurations suggests that our method can be broadly applied across different actuator designs. We believe that as long as the actuator is sufficiently soft and self-drivable, our method is expected to perform effectively, requiring only a new characterization process.

In summary, with two sensors on the dorsal sides of SEMPA, there are four possible patterns of sensor readings, which can be learned to distinguish three types of contact:

1. $R1$ increase, $R2$ decrease (lateral contact in the positive direction).
2. $R2$ increase, $R1$ decrease (lateral contact in the negative direction).
3. Both increase (twist contact).
4. Both decrease (front contact).

Compound contact. The three types of contacts discussed above are based on the assumption that the SEMPA was initially in a free-bending state. However, even if the SEMPA is already in contact with an object, it can detect new contacts if it reaches a new steady state (where the sensors' readings have stabilized). By tracking the change in resistance from any given steady state, any deviation beyond a predetermined threshold indicates a change in state, which can be perceived as another contact. With that, the HICI can perceive multiple contacts in a time sequence. We discuss this further in the case study section.

Free-bending model

To demonstrate the feasibility of HICI in soft robot proprioception, we developed a data-driven model to estimate the pose of SEMPA during free bending, determining its tip position and orientation. This model calculates free-bending pose, and we apply our HICI method to estimate the perturbed pose of the soft robot.

We also account for the influence of gravity by incorporating the base orientation of SEMPA into the model. The base orientation of the finger (orientation of the rigid support hardware on which the actuator is mounted, orange components in Figure 1, not considering deflection of the SEMPA due to gravity, actuation, or external perturbation) is represented by two angles, θ(0–180° rotation about the global y-axis) and α (0–360° rotation about the finger z-axis) (Fig. 5A (i)). With 45° increments, we considered a total of 26 base orientations (see Supplementary Data). The base orientation $\theta = 0°$ occurs when the SEMPA points downward (as shown in Fig. 4). See further discussion in Supplementary Data S1 and Supplementary Fig. S5. The base orientation shown in Figure 5A (i) is $\theta = 90°$, $\alpha = 0°$. We collected all marker data to develop the model using an Optitrack motion capture system with 15 cameras. We installed six markers on the finger, as shown in Figure 5A (ii), with markers $M4$, $M5$, and $M6$ representing the SEMPA tip. During data collection, we varied the input pressures of each channel from 0 to 40 kPa to induce different bending configurations, recording the sensors' resistances ($R1$, $R2$) (summary plot in Fig. 5B, details in Supplementary Data) and the position of the markers (x, y, z) (three configurations in Fig. 5C, the remainder in Supplementary Data). Using MATLAB, we developed a 10th-order polynomial regression model. Given pressure

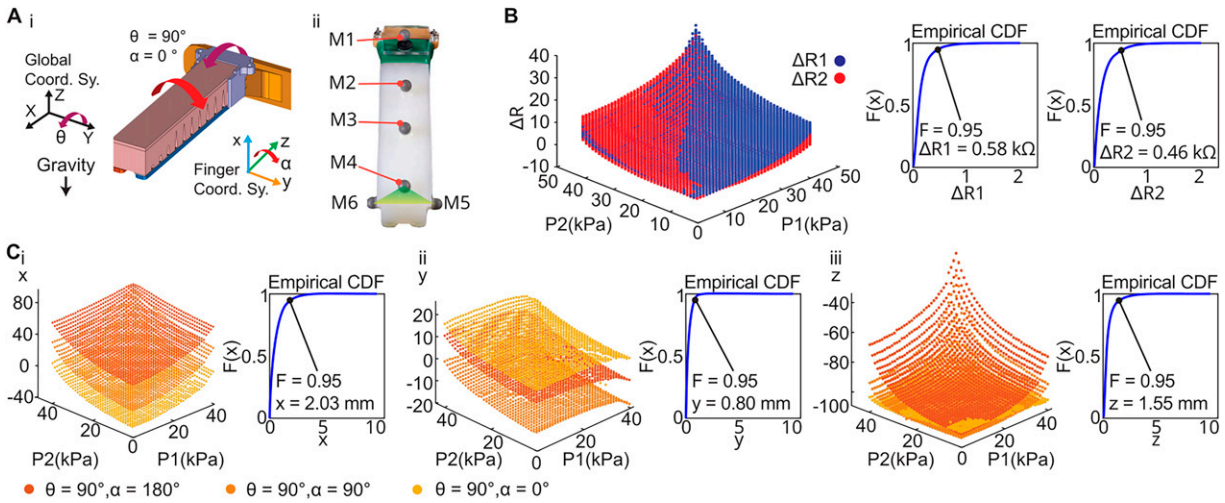

FIG. 5. Free bending model. **(A)** Nomenclature. **(i)** Variables and coordinate system. **(ii)** Marker configuration. **(B)** Plot of sensors' responses for all 26 considered base orientations, followed by the CDF plot of $R1$ and $R2$, showing the accuracy of the derived resistance estimation equations. **(C)** Plot of marker $M6$ position (x, y, z) for 3 of 26 base orientations, showing the influence of gravity and CDF plot of x, y, and z, demonstrating the accuracy of the data-driven pose estimation model.

state and finger base orientation ($P1$, $P2$, θ, α) as inputs, the model outputs an estimate of the tip position (x, y, z) and sensor resistances ($R1$, $R2$). Each output variable, such as the x-coordinate, is represented by a separate 10th-order polynomial equation. Data were collected 2x for each configuration. The initial data set was used to generate the model, and the second set was used to evaluate the accuracy (cumulative distribution function [CDF] and threshold).

Threshold. We would like to find a threshold value for $\Delta R1$ and $\Delta R2$, above which deviation from reference resistance indicates the presence of an external perturbing force. We generated a CDF plot of the error between the model and the real data for each variable. The CDF analysis of position demonstrates that for all input pressures ($P1$, $P2$, $\in$ 0–40 kPa) and base orientations (θ, α), 95% of the time, marker position was within 2 mm of the expected position in all directions (x, y, and z) (Fig. 5C). Further, the CDF analysis of sensor responses demonstrates that for the same inputs, 95% of the time, both sensor resistances are within 0.6 kΩ of the values predicted by the model (Fig. 5B). We selected a threshold value with a multiplier of 0.8 kΩ, 1.3 times this 95% value. Based on the application, a larger or smaller multiplier can be chosen to avoid false positives or negatives, respectively. Thus, for the remainder of this work, we define a deviation in both $R1$ and $R2$ from the predicted model value of 0.8 kΩ as contact.

Pose estimation in free bending and multimode contact

The model developed in the previous section estimates the pose of the SEMPA in free bending based on input pressures and base orientation, and it gives us anticipated resistance values $R1$ and $R2$. We have developed a resistance threshold value of 0.8 kΩ, beyond which we identify the system as having transitioned from free bending to a state of contact. When contact is detected, we utilize our HICI method to determine the mode and magnitude of external contact, and we update the pose estimation accordingly. By analyzing the difference between the real-time $R1$ and $R2$ and the corresponding reference values, we can estimate the deviation or rotating angle of the SEMPA tip using the corresponding second-order equations. With the theoretical pose information of SEMPA in free bending, we can refine this estimation to include contact-based deformation by either adding a distance vector or multiplying by a rotation matrix to achieve an updated pose estimation (Fig. 6A). We demonstrated this methodology by developing a SEMPA pose tracking program, as shown in Figure 6A. During the demonstration, the sensors' responses followed the patterns we identified earlier, as illustrated in Figure 6B. See also Supplementary Video S1.

Case study

To demonstrate the generalizability of HICI and its potential to boost the control of soft robots in real applications, we developed a two-finger gripper incorporating two SEMPA units (Fig. 7A). This gripper can perceive external contact during free bending, distinguish between different perturbations, and respond accordingly. As shown in the finite state machine

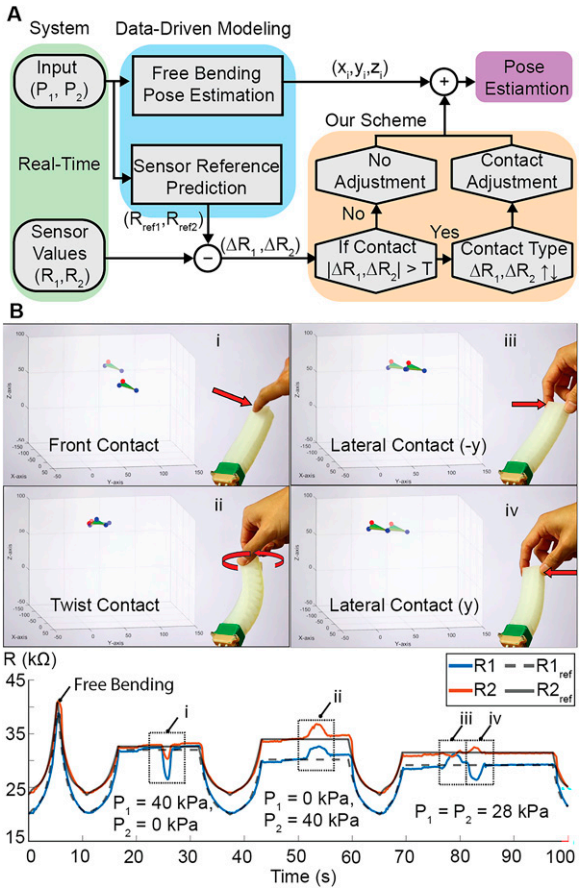

FIG. 6. Estimating pose: free bending and contact (front, lateral, and twist). **(A)** Flowchart for the real-time proprioception of SEMPA in both free bending and contact cases. **(B)** Screenshots from the demonstration (Supplementary Video SV1) with pose estimates of the tip: unperturbed (*light*) and perturbed (*bold*), under different contact modes. The plot at the bottom demonstrates resistance responses versus time for both sensors. When both sensors deviate from reference values beyond the threshold, contact is identified, and the algorithm adds a perturbation correction factor to pose estimation.

(Fig. 7B) and the sensor response curve (Fig. 7C), the gripper initially inflates to close (State 1). If contact is detected (change in all four sensors' resistance exceeding the threshold, Tof ±0.8 kΩ, the gripper grips the cup (P_i = 35 kPa) (State 2) and raises it. If no contact is detected, the gripper opens and recloses, repeating this process until it senses a contact.

While holding the cup (State 2), the gripper is able to detect and respond to external perturbations. We tested three distinct perturbations induced by external forces. Each perturbation results in a distinct change in the embedded sensors' resistances, providing sufficient information to differentiate them from each other (Fig. 7C).

i. *Snatch the cup (F global x)*: An external force attempts to remove the cup from the gripper along the global x-axis. All four sensor responses decrease ($\Delta R_{1-4} < -T$). Controller transitions to State 3.
ii. *Weight added to the cup (–F global z)*: An additional 115 g is added to the cup. All four sensor responses increase ($\Delta R_{1-4} > T$). Controller transitions to State 4.

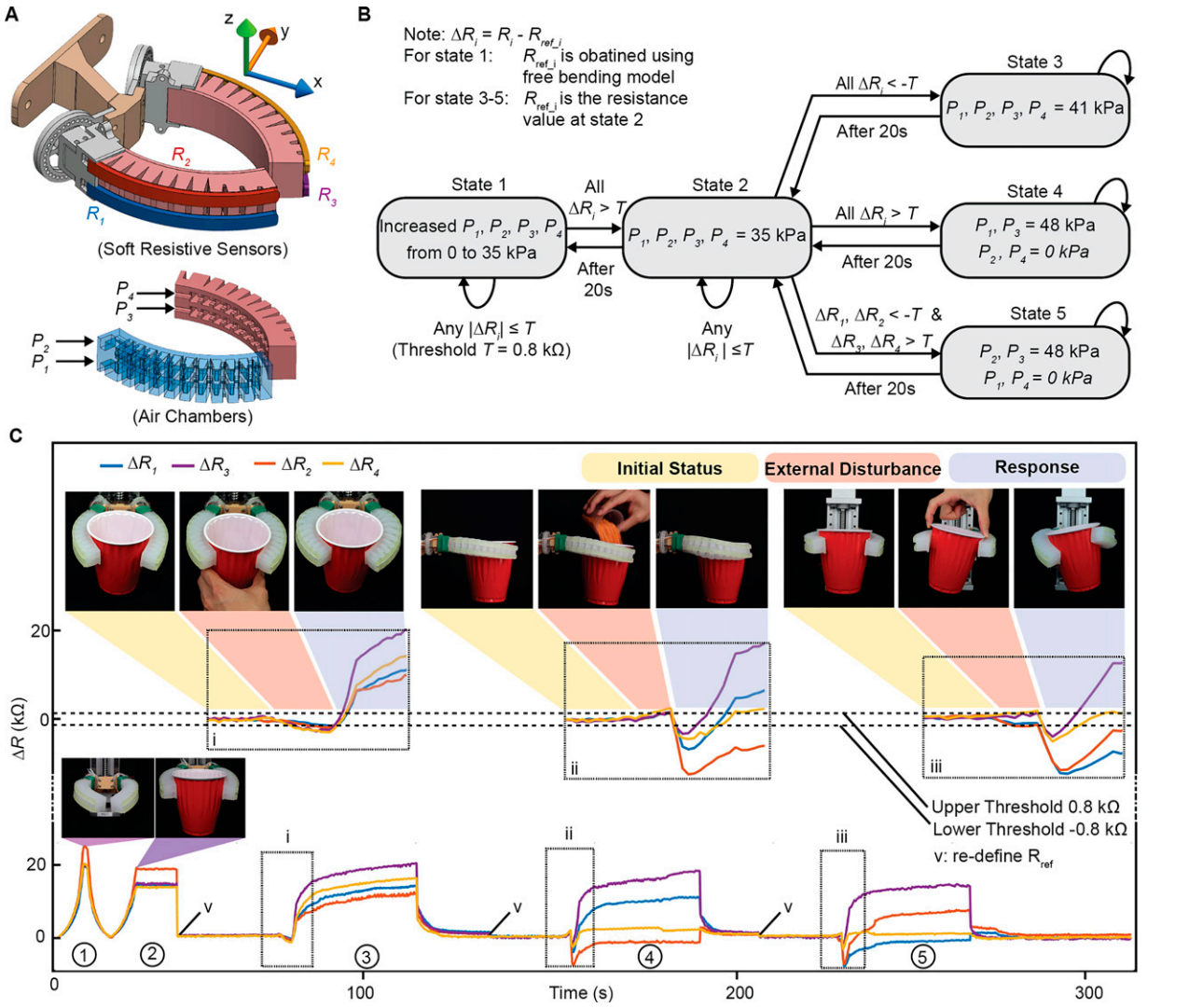

FIG. 7. Two-finger gripper case study. **(A)** Nomenclature of the two SEMPA gripper. Pressure, sensor numbering, and global coordinate system. **(B)** A finite state machine diagram of the case study. **(C)** The sensors' resistances plot throughout the entire case study. Circled numbers below sensor response curves correspond to states numbers in state machine B. Sensor ΔR_i values correlate to nomenclature in A (inset stills from Supplementary Video SV6).

iii. *Tilt the cup (M global x)*: A moment is applied by hand, attempting to twist the cup (applying moment around the global $-x$ direction). Two sensor responses increase, and two decrease ($\Delta R_{1,2} < -T$, $\Delta R_{3,4} > T$). Controller transitions to State 5.

Note that these patterns occur when the finger is already in contact with the cup, not during free bending, so they do not directly match the patterns identified in the contact distinction section. However, this demonstrates that our HICI method can detect not only a single contact but also multiple contacts in sequence. Once the sensor value stabilizes under one contact, a subsequent contact causes the sensor value to deviate from the steady state, providing additional information to identify the new contact.

When the gripper has identified an external perturbation and transitioned to State 3, 4, or 5, the gripper responds by varying pressure states of its internal air chambers (P1 to P4), generating out-of-plane force to counteract the external perturbation and maintain the cup's posture (Fig. 7C). After 20 s, the gripper returns to State 2. External perturbation and gripper restoring force may alter gripping pose; thus, sensor resistances (R_{ref}) may not return to initial values. Thus, upon returning to State 2, the controller recalibrates to current R_{ref} values for future ΔR_i calculations (Fig. 7C, notations v). If the gripper remains in State 2 for greater than 15 s, it returns to State 1 (see Supplementary Video S6).

Materials and Methods

Fabrication

To fabricate a SEMPA, we employed a sequential layer molding method.[46] We cast each component of the sensors (Ecoflex 30 Silicone) and actuator (Dragon Skin 10 Silicone) individually, and we bonded the layers together using Ecoflex 30 Silicone as an adhesive (Smooth-On, Macungie, PA, USA) (Fig. 8). We incorporated a thin layer

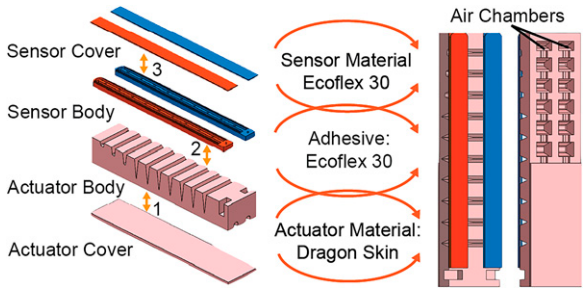

FIG. 8. An overview of the molding and sequential bonding (Steps 1, 2, and 3) manufacturing process of SEMPA (*left*) and illustration of its internal structure (*right*).

of fabric-like mesh into the actuator cover layer during the casting process. This flexible but inextensible layer limited strain in that region, causing the finger to bend upon inflation. The molds were designed using Solidworks software (Desault Systemes, Waltham, MA, USA) and 3D printed using a Formlabs printer (Formlabs, Somerville, MA, USA). Following the attachment of the sensors to the actuator, we injected the 1-ethyl-3-methylimidazolium ethyl sulfate into the sensor channels using syringes. This ionic liquid is used as a soft sensor conductor due to its low vapor pressure and nonpermeability through elastomeric matrices.

Contact detection

Front contact. To determine the relationship between changes in sensor resistance and tip displacement, we recorded sensor values as we displaced the tip of the SEMPA using an external bracket (small aluminum bracket mounted to a translation stage). With the SEMPA oriented downward (Fig. 4A), we moved the bracket along the negative x-axis from $x = 30$ mm to $x = 0$ mm and back to $x = 30$ mm at a rate of 0.5 mm/s. The SEMPA was in free bending with $P1$ set from 10 to 40 kPa in increments of 10 kPa, $P2$ set from 10 to 40 kPa in increments of 10 kPa, and both $P1$ and $P2$ set from 10 to 40 kPa in increments of 10 kPa. During the process, the height of the bracket was maintained constant. To characterize contact location (in the z-direction), we used a similar procedure. However, here the distance from the bracket to the SEMPA along the x-axis was maintained constant, and we moved the bracket along the z-axis from an initial position (25 mm from the base) to the tip of the SEMPA (Fig. 4B) and back to the starting position at a rate of 1.5 mm/s. During the process, we recorded the sensor's values and used MATLAB to find a regression equation.

Lateral contact. We collected sensor readings while we subjected the SEMPA to an external displacement along the y-axis using the external bracket described above. We imposed a displacement of the SEMPA tip of 30 mm in the $\pm y$ direction, back to the initial position, followed by 30 mm along the $-y$ direction, and then back to the initial position (Fig. 4C) at a rate of 0.33 mm/s. We conducted the experiments under the same base orientation and pressure conditions applied in front contact characterization.

Twist contact. We collected sensor readings while the tip of the SEMPA was subjected to an external rotation about the z-axis. We imposed this rotation by sandwiching the tip of the SEMPA between two aluminum brackets, which were mounted to a rotation stage. The axis of rotation of the stage was coincident with the centerline of the SEMPA. We rotated the tip of SEMPA –90° about its centerline, returned to the initial position, twisted –90° about the rotation axis, and then returned to the initial position at a rate of 1°/s. We conducted the experiments under the same base orientation and pressure conditions applied in front contact characterization.

Free bending modeling

In each of 26 base orientations, the SEMPA was given pressure inputs to bend freely with 36 different $P1$ values and 36 different $P2$ values (see Supplementary Data S2). Initially, $P2$ was maintained at 0 kPa while P1 was inflated from 0 to 40 kPa in increments of 1.14 kPa. This process was repeated 35 more times while maintaining $P2$ at 1.14, 2.28, ... 40 kPa in increment of 1.14 kPa. During this process, we used a motion capture system (Optitrack) to record the position of each marker, and we recorded pressure inputs ($P1$, $P2$) and sensor outputs ($R1$, $R2$) using the system shown in Figure 2. From these data, we established a matrix of output values: (x, y, z) positions and $R1$, $R2$ values for each input pressure state: $P1$, $P2$ values for pressures from 0 to 40 kPa for each recorded combination of $P1$, $P2$ (Fig. 5B, C). To determine the threshold, we ran this procedure twice for each base orientation, yielding two sets of data. We used the first set of data to find the regression polynomial model and equation to estimate the pose and sensor values in free bending. We used the second set of data to test the model and equation by generating a CDF plot, based on which we picked our threshold value for contact detection (CDF insets, Fig. 5).

Case study

We built a gripper using two SEMPA actuators connected with 3D-printed brackets (Form 3, Formlabs) and commercial fasteners. We attached the gripper to a vertical linear stage (Fig. 1A, lower left) controlled by Arduino to move up and down. Once the gripper sensed contact (as described in the Results section), the linear stage was triggered to lift the gripper and wait for the sensors' responses. Translation stage and gripper behavior are regulated by logic states of a finite state machine (Fig. 7B). The gripper differentiates between perturbation modes based on deviations of the four sensors from anticipated values (threshold as discussed in the Results section) and responds to different perturbation modes with different responses. By focusing on the changes in resistance rather than the absolute values, the gripper can recalibrate at state 2 and subsequently identify new perturbations. By focusing on comparing changes in the four sensors rather than the value of any one sensor, the gripper is able to holistically perceive the mode of external perturbation.

Discussion and Conclusion

In this study, we developed an HICI method that enables a SEMPA to self-sense and perceive the mode of external

perturbations and estimate the resulting displacement. We characterized the responses of the SMEPA's two onboard resistive sensors to front, lateral, and twist contacts during free-bending at various input pressures. We developed a data-driven pose estimation model for the SEMPA in free bending in 26 base orientations (to account for gravity). We generated a matrix transform method to account for the deformation caused by external contact. We augmented the free-bending model with the matrix transform to estimate the perturbed pose of the SEMPA under front, lateral, and twist contact. This integration allowed us to achieve real-time proprioception of 2 DOF soft robot actuator. To further demonstrate the effectiveness of this soft robot's proprioception method in control work, we designed a two-finger gripper capable of identifying and responding to different perturbations while gripping a cup.

The main purpose of this work was to demonstrate the feasibility of the HICI method in the proprioception and control of soft robots. The single-finger SEMPA and two-finger gripper provided compelling demonstrations of this method during the flexion portion of the flexion–relaxation cycle in static and quasistatic conditions. Further development is desirable to extend its application to dynamic scenarios, where contacts occur during high-speed movement including dynamic effects. This could involve incorporating a hysteresis solver into the current framework to address the sensors' response delays.

Further development could also explore applying the HICI method on a more complex robot (perhaps a quadrupedal walker) to perceive a more complex soft robot geometry and handle multiple simultaneous contacts. This complexity can be alleviated by incorporating additional sensors and employing a classification neural network to interpret the sensors' response patterns that exceed human analytical capabilities. The ultimate goal is to integrate this novel method into closed-loop feedback control on a soft robot, enabling it to perceive and respond to events such as force control in human–robot interactions or obstacle-aware trajectory optimization. This article lays the groundwork for such future advancements. The HICI method can be used on any soft robot, which includes (or could be made to incorporate) multiple deformation sensors.

The field of soft robotics has long sought a robust method of closed-loop control but has yet to converge on a generally accepted solution. In order to control a soft robot, we must first have a reliable perception of its pose (in free bending and under all likely external perturbations). Not constrained to one type of physical system or underlying controller, this approach can be used by many soft robots searching for a robust means of proprioception.

Authors' Contributions

S.W.: Conceptualization (equal), investigation (lead), methodology (equal), software, validation, data curation, and writing—original draft. K.-Y.L.: Conceptualization (equal) and investigation (supporting). X.X.: Methodology (equal), project administration, and supervision. M.W.: Conceptualization (equal), methodology (equal), project administration, supervision, and writing—review and editing.

Author Disclosure Statement

No competing or financial interests exist.

Funding Information

This work was supported in part by the University of Wisconsin-Madison Office of the Vice Chancellor for Research and Graduate Education funded by the Wisconsin Alumni Research Foundation.

Supplementary Material

Supplementary Data S1
Supplementary Data S2
Supplementary Figure S1
Supplementary Figure S2
Supplementary Figure S3
Supplementary Figure S4
Supplementary Figure S5
Supplementary Figure S6
Supplementary Figure S7
Supplementary Video S1
Supplementary Video S2
Supplementary Video S3
Supplementary Video S4
Supplementary Video S5
Supplementary Video S6

Reference

1. Marchese AD, Katzschmann RK, Rus D. A recipe for soft fluidic elastomer robots. Soft Robot 2015;2(1):7–25; doi: 10.1089/soro.2014.0022
2. Zhao Y, Xuan C, Qian X, et al. Soft phototactic swimmer based on self-sustained hydrogel oscillator. Sci Robot 2019; 4(33):eaax7112; doi: 10.1126/scirobotics.aax7112
3. Terryn S, Langenbach J, Roels E, et al. A review on self-healing polymers for soft robotics. Materials Today 2021; 47:187–205; doi: 10.1016/j.mattod.2021.01.009
4. Xiong J, Chen J, Lee PS. Functional fibers and fabrics for soft robotics, wearables, and human–robot interface. Advanced Materials 2021;33(19):2002640; doi: 10.1002/adma.202002640
5. Laschi C, Mazzolai B, Cianchetti M. Soft robotics: Technologies and systems pushing the boundaries of robot abilities. Sci Robot 2016;1(1):eaah3690; doi: 10.1126/scirobotics.aah3690
6. Polygerinos P, Correll N, Morin SA, et al. Soft robotics: Review of fluid-driven intrinsically soft devices; manufacturing, sensing, control, and applications in human-robot interaction. Adv Eng Mater 2017;19(12):1700016; doi: 10.1002/adem.201700016
7. Hawkes EW, Blumenschein LH, Greer JD, et al. A soft robot that navigates its environment through growth. Sci Robot 2017;2(8):eaan3028; doi: 10.1126/scirobotics.aan3028
8. Cianchetti M, Laschi C, Menciassi A, et al. Biomedical applications of soft robotics. Nat Rev Mater 2018;3(6): 143–153; doi: 10.1038/s41578-018-0022-y
9. Polygerinos P, Wang Z, Galloway KC, et al. Soft robotic glove for combined assistance and at-home rehabilitation. Robotics and Autonomous Systems 2015;73:135–143; doi: 10.1016/j.robot.2014.08.014

10. Li M, Pal A, Aghakhani A, et al. Soft actuators for real-world applications. Nat Rev Mater 2022;7:235–249; doi: 10.1038/s41578-021-00389-7
11. Iida F, Laschi C. Soft Robotics: Challenges and perspectives. Procedia Computer Science 2011;7:99–102; doi: 10.1016/j.procs.2011.12.030
12. Tuthill JC, Azim E. Proprioception. Curr Biol 2018;28(5):R194–R203; doi: 10.1016/j.cub.2018.01.064
13. Rus D, Tolley MT. Design, fabrication and control of soft robots. Nature 2015;521(7553):467–475; doi: 10.1038/nature14543
14. Armanini C, Boyer F, Mathew AT, et al. Soft robots modeling: A structured overview. IEEE Trans Robot 2023;39(3):1728–1748; doi: 10.1109/TRO.2022.3231360
15. Della Santina C, Duriez C, Rus D. Model-Based control of soft robots: A survey of the state of the art and open challenges. IEEE Control Syst 2023;43(3):30–65; doi: 10.1109/MCS.2023.3253419
16. Troeung C, Liu S, Chen C. Modelling of tendon-driven continuum robot based on constraint analysis and pseudo-rigid body model. IEEE Robot Autom Lett 2023;8(2):989–996; doi: 10.1109/LRA.2023.3234821
17. Satheeshbabu S, Krishnan G. Designing systems of fiber reinforced pneumatic actuators using a pseudo-rigid body model. In: 2017 IEEE/RSJ International Conference on Intelligent Robots and Systems (IROS) 2017; pp. 1201–1206; doi: 10.1109/IROS.2017.8202292
18. Till J, Aloi V, Rucker C. Real-time dynamics of soft and continuum robots based on Cosserat rod models. The International Journal of Robotics Research 2019;38(6):723–746; doi: 10.1177/0278364919842269
19. Webster RJ, Jones BA. Design and kinematic modeling of constant curvature continuum robots: A review. The International Journal of Robotics Research 2010;29(13):1661–1683; doi: 10.1177/0278364910368147
20. Godage IS, Medrano-Cerda GA, Branson DT, et al. Modal kinematics for multisection continuum arms. Bioinspir Biomim 2015;10(3):35002; doi: 10.1088/1748-3190/10/3/035002
21. Della Santina C, Bicchi A, Rus D. On an improved state parametrization for soft robots with piecewise constant curvature and its use in model based control. IEEE Robot Autom Lett 2020;5(2):1001–1008; doi: 10.1109/LRA.2020.2967269
22. Stella F, Guan Q, Della Santina C, et al. Piecewise affine curvature model: A reduced-order model for soft robot-environment interaction beyond PCC. In: 2023 IEEE International Conference on Soft Robotics (RoboSoft) 2023; pp. 1–7; doi: 10.1109/RoboSoft55895.2023.10121939
23. Della Santina C, Katzschmann RK, Biechi A, et al. Dynamic control of soft robots interacting with the environment. In: 2018 IEEE International Conference on Soft Robotics (RoboSoft) 2018; pp. 46–53; doi: 10.1109/ROBOSOFT.2018.8404895
24. Ferrentino P, Tabrizian SK, Brancart J, et al. FEA-Based inverse kinematic control: Hyperelastic material characterization of self-healing soft robots. IEEE Robot Automat Mag 2022;29(3):78–88; doi: 10.1109/MRA.2021.3132803
25. Xavier MS, Fleming AJ, Yong YK. Finite element modeling of soft fluidic actuators: Overview and recent developments. Advanced Intelligent Systems 2021;3(2):2000187; doi: 10.1002/aisy.202000187
26. Polygerinos P, Wang Z, Overvelde JTB, et al. Modeling of soft fiber-reinforced bending actuators. IEEE Trans Robot 2015;31(3):778–789; doi: 10.1109/TRO.2015.2428504
27. Duriez C. Control of elastic soft robots based on real-time finite element method. In: 2013 IEEE International Conference on Robotics and Automation 2013; pp. 3982–3987; doi: 10.1109/ICRA.2013.6631138
28. Chenevier J, González D, Aguado JV, et al. Reduced-order modeling of soft robots. PLoS One 2018;13(2):e0192052; doi: 10.1371/journal.pone.0192052
29. Goury O, Duriez C. Fast, generic, and reliable control and simulation of soft robots using model order reduction. IEEE Trans Robot 2018;34(6):1565–1576; doi: 10.1109/TRO.2018.2861900
30. Qin L, Peng H, Huang X, et al. Modeling and simulation of dynamics in soft robotics: A review of numerical approaches. Curr Robot Rep 2023;5(1):1–13; doi: 10.1007/s43154-023-00105-z
31. Chen Z, Renda F, Gall AL, et al. Data-Driven methods applied to soft robot modeling and control: A review. IEEE Trans Automat Sci Eng 2025;22:2241–2256; doi: 10.1109/TASE.2024.3377291
32. Shih B, Shah D, Li J, et al. Electronic skins and machine learning for intelligent soft robots. Sci Robot 2020;5(41):eaaz9239; doi: 10.1126/scirobotics.aaz9239
33. Sefati S, Hegeman R, Alambeigi F, et al. FBG-Based position estimation of highly deformable continuum manipulators: Model-Dependent vs. Data-Driven approaches. In: 2019 International Symposium on Medical Robotics (ISMR) 2019; pp. 1–6; doi: 10.1109/ISMR.2019.8710179
34. Loutfi IM, Boutchouang AHB, Melingui A, et al. Learning-Based approaches for forward kinematic modeling of continuum manipulators. IFAC-PapersOnLine 2020;53(2):9899–9904; doi: 10.1016/j.ifacol.2020.12.2697
35. Fang G, Wang X, Wang K, et al. Vision-Based online learning kinematic control for soft robots using local gaussian process regression. IEEE Robot Autom Lett 2019;4(2):1194–1201; doi: 10.1109/LRA.2019.2893691
36. Soter G, Conn A, Hauser H, et al. Bodily aware soft robots: Integration of proprioceptive and exteroceptive sensors. In: 2018 IEEE International Conference on Robotics and Automation (ICRA) 2018; pp. 2448–2453; doi: 10.1109/ICRA.2018.8463169
37. Wang H, Totaro M, Beccai L. Toward perceptive soft robots: Progress and challenges. Adv Sci (Weinh) 2018;5(9):1800541; doi: 10.1002/advs.201800541
38. Hegde C, Su J, Tan JMR, et al. Sensing in soft robotics. ACS Nano 2023;17(16):15277–15307; doi: 10.1021/acsnano.3c04089
39. Wall V, Zöller G, Brock O. A method for sensorizing soft actuators and its application to the RBO hand 2. In: 2017 IEEE International Conference on Robotics and Automation (ICRA) 2017; pp. 4965–4970; doi: 10.1109/ICRA.2017.7989577
40. Truby RL, Wehner M, Grosskopf AK, et al. Soft Somatosensitive actuators via embedded 3D printing. Adv Mater 2018;30(15):e1706383; doi: 10.1002/adma.201706383
41. Morrow J, Shin H-S, Phillips-Grafflin C, et al. Improving soft pneumatic actuator fingers through integration of soft sensors, position and force control, and rigid fingernails. In: 2016 IEEE International Conference on Robotics and Automation (ICRA) IEEE; 2016; pp. 5024–5031.

42. Farrow N, McIntire L, Correll N. Functionalized textiles for interactive soft robotics. In: 2017 IEEE International Conference on Robotics and Automation (ICRA) 2017; pp. 5525–5531; doi: 10.1109/ICRA.2017.7989651
43. Zhang H, Wang M. Multi-Axis soft sensors based on dielectric elastomer. Soft Robotics 2016;3(1):3–12; doi: 10.1089/soro.2015.0017
44. Sareh S, Noh Y, Li M, et al. Macrobend optical sensing for pose measurement in soft robot arms. Smart Mater Struct 2015;24(12):125024; doi: 10.1088/0964-1726/24/12/125024
45. Sareh S, Jiang A, Faragasso A, et al. Bio-Inspired tactile sensor sleeve for surgical soft manipulators. In: 2014 IEEE International Conference on Robotics and Automation (ICRA) 2014; pp. 1454–1459; doi: 10.1109/ICRA.2014.6907043
46. Park Y-L, Chen B-R, Wood RJ. Design and fabrication of soft artificial skin using embedded microchannels and liquid conductors. IEEE Sensors J 2012;12(8):2711–2718; doi: 10.1109/JSEN.2012.2200790
47. Viry L, Levi A, Totaro M, et al. Flexible three-axial force sensor for soft and highly sensitive artificial touch. Adv Mater 2014;26(17):2659–2664, 2614; doi: 10.1002/adma.201305064
48. Din S, Xu W, Cheng LK, et al. A stretchable multimodal sensor for soft robotic applications. IEEE Sensors J 2017;17(17):5678–5686; doi: 10.1109/JSEN.2017.2726099
49. Ge J, Sun L, Zhang F-R, et al. A stretchable electronic fabric artificial skin with pressure-, lateral strain-, and flexion-sensitive properties. Adv Mater 2016;28(4):722–728; doi: 10.1002/adma.201504239
50. Gariya N, Kumar S, Shaikh A, et al. A review on soft pneumatic actuators with integrated or embedded soft sensors. Sensors and Actuators A: Physical 2024;372:115364; doi: 10.1016/j.sna.2024.115364
51. Wang P, Xie Z, Xin W, et al. Sensing expectation enables simultaneous proprioception and contact detection in an intelligent soft continuum robot. Nat Commun 2024;15(1):9978; doi: 10.1038/s41467-024-54327-6
52. Boivin M, Milutinović D, Wehner M. Movement error based control for a firm touch of a soft somatosensitive actuator. In: 2019 American Control Conference (ACC) 2019; pp. 7–12; doi: 10.23919/ACC.2019.8815142
53. Boivin M, Wehner M, Milutinović D. Compliant proprioceptive touch without a force sensor: A kinesthetic feedback control approach. In: 2022 IEEE Conference on Control Technology and Applications (CCTA) 2022; pp. 455–461; doi: 10.1109/CCTA49430.2022.9966195
54. Boivin M, Esch C, Wehner M, et al. Feedback control for inflatable soft robotic finger touch detection based on static pressure-resistance characteristics. In: 2023 American Control Conference (ACC) San Diego, CA, USA; 2023; pp. 159–164; doi: 10.23919/ACC55779.2023.10155854
55. Boivin M, Lin K-Y, Wehner M, et al. Proprioceptive touch of a soft actuator containing an embedded intrinsically soft sensor using kinesthetic feedback. J Intell Robot Syst 2023;107(2):28; doi: 10.1007/s10846-023-01815-4
56. Wirekoh J, Valle L, Pol N, et al. Sensorized, flat, pneumatic artificial muscle embedded with biomimetic microfluidic sensors for proprioceptive feedback. Soft Robot 2019;6(6):768–777; doi: 10.1089/soro.2018.0110
57. Jung J, Park M, Kim D, et al. Optically Sensorized elastomer air chamber for proprioceptive sensing of soft pneumatic actuators. IEEE Robot Autom Lett 2020;5(2):2333–2340; doi: 10.1109/LRA.2020.2970984
58. Kim H, Na H, Noh S, et al. Inherently integrated microfiber-based flexible proprioceptive sensor for feedback-controlled soft actuators. Npj Flex Electron 2024;8(1):15; doi: 10.1038/s41528-024-00302-6
59. Li MS, Huh TM, Yahnker CR, et al. Resonant pneumatic tactile sensing for soft grippers. IEEE Robot Autom Lett 2022;7(4):10105–10111; doi: 10.1109/LRA.2022.3191186
60. Zöller G, Wall V, Brock O. Active acoustic contact sensing for soft pneumatic actuators. In: 2020 IEEE International Conference on Robotics and Automation (ICRA) 2020; pp. 7966–7972; doi: 10.1109/ICRA40945.2020.9196916
61. Loo JY, Ding ZY, Baskaran VM, et al. Robust multimodal indirect sensing for soft robots via neural network-aided filter-based estimation. Soft Robot 2022;9(3):591–612; doi: 10.1089/soro.2020.0024
62. She Y, Liu SQ, Yu P, et al. Exoskeleton-Covered soft finger with vision-based proprioception and tactile sensing. arXiv 2019; doi: 10.48550/ARXIV.1910.01287
63. Scimeca L, Hughes J, Maiolino P, et al. Model-Free Soft-Structure reconstruction for proprioception using tactile arrays. IEEE Robot Autom Lett 2019;4(3):2479–2484; doi: 10.1109/LRA.2019.2906548
64. Preechayasomboon P, Rombokas E. Sensuator: A hybrid sensor–actuator approach to soft robotic proprioception using recurrent neural networks. Actuators 2021;10(2):30; doi: 10.3390/act10020030
65. Wehner M, Truby RL, Fitzgerald DJ, et al. An integrated design and fabrication strategy for entirely soft, autonomous robots. Nature 2016;536(7617):451–455.
66. Laschi C. Embodied Intelligence in soft robotics: Joys and sorrows. IOP Conf Ser: Mater Sci Eng 2022;1261(1):12002; doi: 10.1088/1757-899X/1261/1/012002
67. Laschi C, Cianchetti M. Soft robotics: New perspectives for robot bodyware and control. Front Bioeng Biotechnol 2014;2:3.
68. Walker J, Zidek T, Harbel C, et al. Soft robotics: A review of recent developments of pneumatic soft actuators. Actuators 2020;9(1):3; doi: 10.3390/act9010003
69. Kan Z, Pang C, Zhang Y, et al. Soft actuator with programmable design: Modeling, prototyping, and applications. Soft Robot 2022;9(5):907–925; doi: 10.1089/soro.2020.0148
70. Mosadegh B, Polygerinos P, Keplinger C, et al. Pneumatic networks for soft robotics that actuate rapidly. Adv Funct Materials 2014;24(15):2163–2170; doi: 10.1002/adfm.201303288
71. Zhu Y, Chu K, Chen X, et al. Research and application of a multi-degree-of-freedom soft actuator. Sensors and Actuators A: Physical 2022;338:113492; doi: 10.1016/j.sna.2022.113492
72. Miao Y, Dong W, Du Z. Design of a soft robot with multiple motion patterns using soft pneumatic actuators. IOP Conf Ser: Mater Sci Eng 2017;269:12013; doi: 10.1088/1757-899X/269/1/012013
73. Liu Y, Chen W, Xiong C. Simulation and fabrication of a pneumatic network actuator with capability of bending in multi-planes. In: 2019 IEEE/ASME International Conference on Advanced Intelligent Mechatronics (AIM) 2019; pp. 313–317; doi: 10.1109/AIM.2019.8868457
74. Abondance S, Teeple CB, Wood RJ. A dexterous soft robotic hand for delicate in-hand manipulation. IEEE Robot

Autom Lett 2020;5(4):5502–5509; doi: 10.1109/LRA.2020.3007411
75. Kalisky T, Wang Y, Shih B, et al. Differential pressure control of 3D printed soft fluidic actuators. IEEE Xplore 2017: 6207–6213; doi: 10.1109/IROS.2017.8206523
76. Xiao W, Hu D, Chen W, et al. Modeling and analysis of bending pneumatic artificial muscle with multi-degree of freedom. Smart Mater Struct 2021;30(9):95018; doi: 10.1088/1361-665X/ac1939
77. Xavier MS, Tawk CD, Yong YK, et al. 3D-printed omnidirectional soft pneumatic actuators: Design, modeling and characterization. Sensors and Actuators A: Physical 2021; 332:113199; doi: 10.1016/j.sna.2021.113199
78. Esch C. Construction of Low Cost Multilayered Soft Robots Containing Embedded Intrinsically Soft Sensors. University of California, Santa Cruz ProQuest Dissertations & Theses; 2020.

Address correspondence to:
Michael Wehner
Wehner Engineering
1513 University Ave.
Madison, WI 53706
USA

E-mail: wehner2@wisc.edu